nature physics

LETTERS

https://doi.org/10.1038/s41567-019-0675-5

# Vibrational spectroscopy at atomic resolution with electron impact scattering

Kartik Venkatraman[1], Barnaby D. A. Levin[1], Katia March[2], Peter Rez[3] and Peter A. Crozier[1*]

**Atomic vibrations control all thermally activated processes in materials, including diffusion, heat transport, phase transformations and surface chemistry. Recent developments in scanning transmission electron microscopy (STEM) have enabled nanoscale probing of vibrational modes using electron energy-loss spectroscopy (EELS)[1,2]. Although atomically resolved analysis is routine in STEM, vibrational spectroscopy employing oscillating dipoles yields signals originating from regions tens of nanometres in size, because the scattering angles are only a few microradians[3]. Recently, it has been shown that energy-filtered images recorded at high scattering angles display atomic resolution[4]. Here we show, using conventional on-axis EELS, that non-dipole, impact scattering vibrational signals are present, and exhibit atomic resolution. This on-axis signal shows variations in the spectral peak shape and intensity as the electron probe is scanned across an individual atomic column in a Si sample. Although atomic spatial resolution in coherent elastic scattering will complicate the quantitative interpretation of spectra from crystals, the change in peak shape provides compelling evidence that the vibrational EELS excitation process is highly localized. High spatial resolution is also demonstrated in $SiO_2$, an amorphous polar material. Our approach represents an important technical advance that will provide new insights into the local thermal, elastic and kinetic properties of materials.**

Atomic and molecular heterogeneities such as interfaces, adsorbates and defects (including vacancies, interstitials, dislocations and grain boundaries) often regulate kinetic pathways and are associated with vibrational modes that are substantially different from bulk modes. The jump frequency characterizing kinetic processes is of great practical importance and is determined by local phonon and molecular vibrational modes in a system. Nanoscale vibrational spectroscopy using scanning transmission electron microscopy electron energy-loss spectroscopy (STEM EELS) is already impacting a wide range of important scientific problems, including the measurement of surface and bulk vibrational excitations in MgO nanocubes[5], probing hyperbolic phonon polaritons in hexagonal boron nitride nanoflakes[6], measuring temperature in nanometre-sized areas with 1 K precision[7,8] and determining phonon dispersion in nanoparticles[9]. The delocalized nature of certain vibrational signals allows damage-free nanoscale detection for a variety of organic and inorganic material systems[10–13]. This progress has been impressive, and there is now considerable interest in performing vibrational EELS at atomic resolution. Theoretical treatments have explored the question of spatial resolution[3,14], with some treatments suggesting that atomic-resolution vibrational EELS should be possible[15–18].

A necessary condition to perform atomic-resolution vibrational EELS requires scattered electrons spanning a range of angles up to at least one Bragg angle to interfere[19]. For STEM, this challenge can be addressed by appealing to the reciprocity principle first described by Cowley[20]. In STEM, an electron probe smaller than a (*hkl*) Miller plane spacing can only be formed if the incident electron beam has a convergence semi-angle of at least the Bragg angle. In the sample, momentum transfers will take place across such a probe spanning at least one Bragg angle, leading to interference fringes, ensuring that a high-spatial-resolution signal will be collected by a spectrometer located on the optic axis of the microscope (Fig. 1a). The convergent illumination condition required to create the small probe and achieve high spatial resolution necessarily means the vibrational EELS signal entering the spectrometer will consist of an integral over regions of momentum space spanning more than one Brillouin zone boundary. This is also true for atomic-resolution core-loss EELS and is a consequence of the uncertainty principle.

The vibrational spectrum associated with electron scattering has features in common with both photon and neutron spectroscopies. The electron interactions have been discussed previously in terms of dipole and impact scattering in high-resolution EELS (HREELS) using low-energy incident electrons[21]. Dipole scattering is associated with the long-range Coulomb field, which excites vibrational modes by polarizing the medium, giving spectral features similar to those in infrared (IR) absorption spectroscopy[11,12]. The practical spatial resolution of dipole scattering is on the order of 20–200 Å and can be predicted with classical dielectric theories[22,23]. Electrons may also undergo impact scattering, exciting vibrational modes that appear in neutron scattering but not IR spectroscopy; this includes acoustic modes in all materials, optical modes in non-ionic materials, and symmetric stretching and deformation modes in ionic materials[21]. Impact scattering is associated with short-range interactions and, in principle, should exhibit atomic resolution. A simple way to identify impact modes in EELS is to compare IR, neutron and electron vibrational spectra; impact modes will be present only in the neutron and electron spectra.

A challenge for achieving atomic resolution is to avoid the delocalized dipole signal. For ionic materials, dipole signals, which arise due to asymmetric stretching or deformation modes involving adjacent cations and anions, are much stronger than impact signals[3]. The dipole signal is strongly forward peaked; to avoid this, in previous research the spectrometer entrance aperture outside the probe convergence cone was displaced, achieving a spatial resolution of better than 20 Å (ref. [24]). Others recently extended this approach, showing that energy-filtered images including contributions from acoustic and optical phonons recorded at high scattering angles (>60 mrad) exhibit atomic resolution[4]. The collected EELS signal is always modulated by the elastic scattering signal, which also shows atomic-resolution contrast and complicates the interpretation of variations in energy-filtered image intensities.

[1]School for Engineering of Matter, Transport and Energy, Arizona State University, Tempe, AZ, USA. [2]Eyring Materials Center, Arizona State University, Tempe, AZ, USA. [3]Department of Physics, Arizona State University, Tempe, AZ, USA. *e-mail: crozier@asu.edu

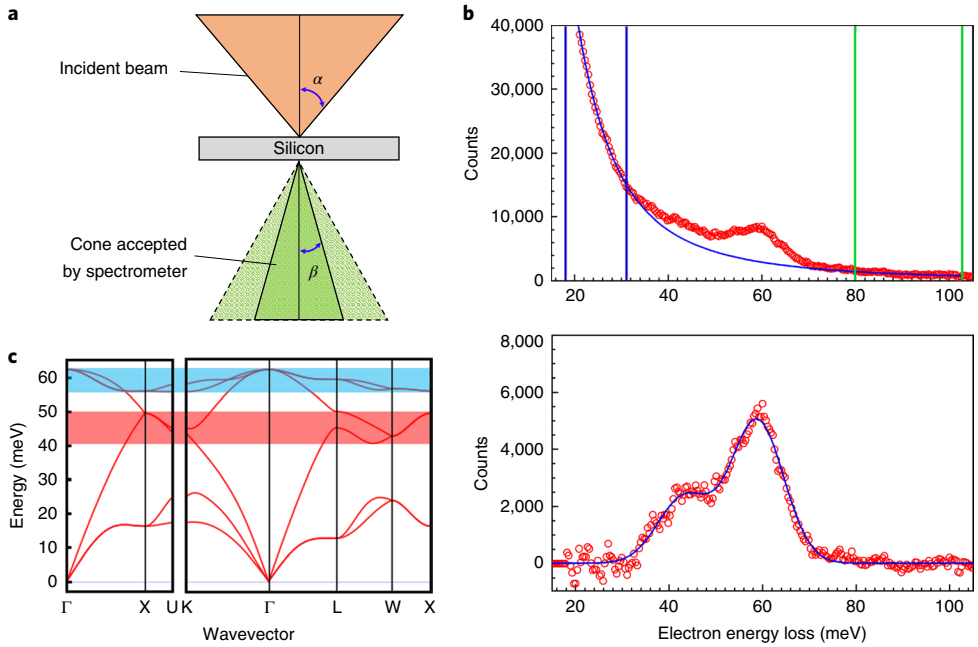


**Fig. 1 | Acquisition geometry and vibrational spectra from silicon. a**, Schematic showing the STEM EELS acquisition geometry used in the experiment, with $\alpha = 28$ mrad and $\beta = 12$ or 24 mrad. **b**, Top: a typical raw vibrational energy-loss spectrum from Si acquired with $\beta = 24$ mrad (red circles). The blue curve shows the background subtraction model employed. The vertical lines (blue and green) show the windows used to fit the background. Bottom: the same spectrum after background subtraction. The blue curve shows the two Gaussian peak fitting model employed, which shows good agreement with the data. **c**, Dispersion surfaces for Si (refs. [25,26]). Blue and red shaded areas correspond to peaks in the density of states on the upper branches from ~55 to 63 meV (optical) and on a lower branch from ~40 to 50 meV (optical and acoustic).

Here, we demonstrate a different approach to avoid the dipole signal that does not require off-axis high scattering angle detection, but instead relies on the presence of specific vibrational modes that can only be excited via highly localized impact scattering. Our approach differs from prior work in several important respects. We employ conventional, on-axis EELS geometry, where the signal is strong. Spectral processing approaches are employed to isolate the impact signal associated with specific vibrational modes from the non-characteristic background and dipole contributions. Approximate corrections are made for the collected elastic signal to minimize ambiguities in the interpretation of the spatial variation of the vibrational signal. We show spatial variations in both the spectral intensity and shape, further demonstrating the sensitivity of the impact peak to the probe position within the unit cell.

We develop and prove the approach initially on Si, a non-ionic elemental semiconductor where impact scattering predominates. For ionic materials we selected $SiO_2$, which shows an impact scattering peak located at a different energy loss from the stronger dipole peaks. Our experiments demonstrate that a localized impact signal in amorphous $SiO_2$ gives high resolution across an $SiO_2$/Si interface.

Figure 1b shows an experimental spectrum from Si, with a strong vibrational peak at ~60 meV and a secondary peak at ~45 meV. In EELS from a thin sample, most incident electrons are not scattered and experience no energy loss, resulting in a very large zero-loss peak (ZLP), and the instrument response function causes this peak to have long tails extending to higher energy loss. Thus, the characteristic vibrational signals sit on a rapidly falling background (Fig. 1b) due to the ZLP tail and non-characteristic losses. This background was modelled and subtracted from the vibrational peaks (for details see Methods; examples are shown in Supplementary Fig. 1). In our experiments, the large, rapidly varying background prevents us from easily detecting and extracting useful signals below ~30 meV, where the background can be almost an order of magnitude greater than at 60 meV. We have therefore chosen to focus on phonons of energy >30 meV. In the future, characterization of phonons of <30 meV will become more practical as further improvements in energy resolution in vibrational EELS reduce the width of the ZLP, and therefore reduce the background.

The intensity and shape of the phonon spectra can be expressed as a product of a projected density of states and a position-dependent dynamical form factor. A theoretical description of electron scattering by phonons along with a schematic showing the scattering geometry are provided in the Methods and Supplementary Fig. 2. Qualitative insights on the origin of spectral features can be ascertained from the phonon dispersion curves for Si (reproduced in Fig. 1c)[25–27]. The part of the phonon dispersion surface sampled during our experiment is associated with a cross-section of the Brillouin zone orthogonal to the beam direction, as shown in Supplementary Fig. 3. Flat parts of the dispersion curves give rise to maxima in the phonon density of states[28], contributing to stronger spectral intensity. The higher energy peak in the spectrum (~60 meV) is associated with the upper transverse optical branches of the dispersion curves, shaded blue in Fig. 1c, while the lower energy shoulder is associated with longitudinal acoustic and optical modes, shaded red. Contributions from the high and low energy branches to the spectral intensity can be estimated with a simple peak fitting model. Two Gaussians, constrained to widths between 10 and 30 meV, were fitted to background subtracted spectra, with peak positions constrained to lie in the ranges 40–50 meV and 55–63 meV, corresponding to the lower and higher energy bands described above. The two-Gaussian model fits the experimental data well (Fig. 1b).

Inelastic neutron scattering (Supplementary Fig. 4) shows similar features between 40 and 60 meV (ref. [29]), which are not observed with IR spectroscopy, confirming that the signals observed in EELS are associated with impact scattering. To explore the localized nature of the vibrational signals, the spectral intensity was investigated as a function of electron probe position by performing linescans across a Si unit cell. The images in Fig. 2a,b were recorded from

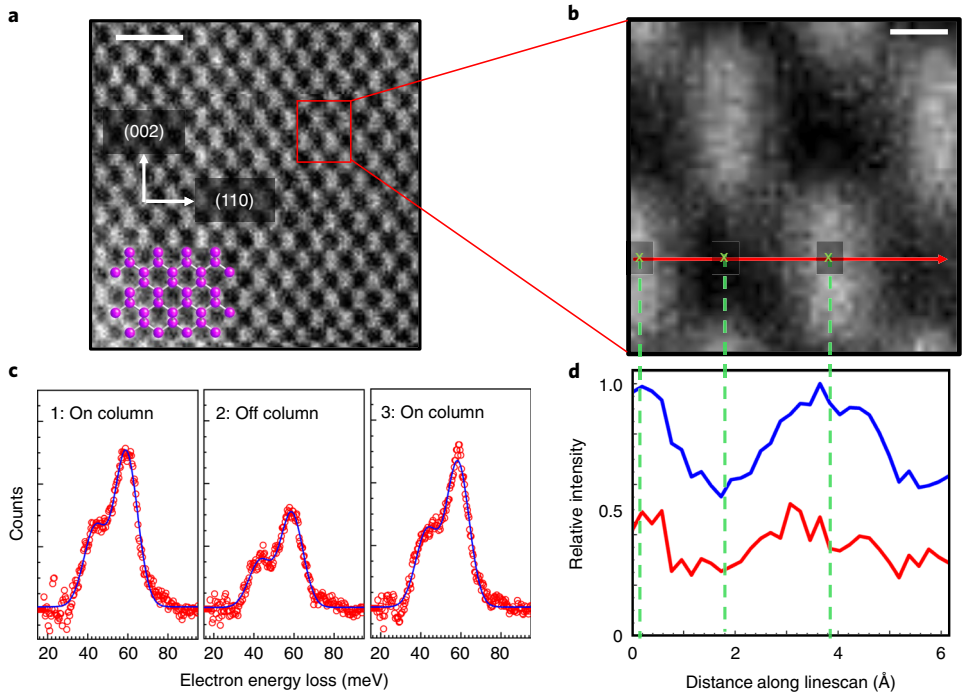


**Fig. 2 | Background subtracted spectra and linescan for large collection angle data. a**, Atomic-resolution annular dark-field (ADF) image with electron-beam monochromation of ~10 meV from Si in [$\bar{1}$10] projection with light contrast corresponding to Si dumbbell column pairs. Scale bar, 10 Å. A model of Si in the [$\bar{1}$10] projection overlaid on the ADF image shows the position of atomic columns that form dumbbells. **b**, Magnified image of the area indicated by a red box in **a**. Scale bar, 1 Å. The red arrow indicates the position and direction of EELS linescan acquisition. **c**, Individual normalized spectra from different positions along the linescan, shown by the green x symbols in **b**. As in Fig. 1, the red circles are experimental data points and the blue line is the result of the Gaussian fit. **d**, The variation in intensity for higher (blue) and lower (red) energy phonons over the linescan indicated in **b**. The profiles are spatially aligned with the ADF image in **b**, as indicated by dashed green guidelines. An increase in phonon intensity can be observed around the dumbbell columns.

Si in the [$\bar{1}$10] projection with the monochromator slit inserted to give 10 meV energy resolution, with a spectrometer entrance aperture corresponding to a 24 mrad collection angle. The total intensity entering the spectrometer passes through minima and maxima as the probe moves on and off the atomic columns, primarily due to interference effects associated with the phase contrast elastic bright-field signal. To correct approximately for these interference effects, each spectrum in the linescan was normalized to the total intensity entering the spectrometer. One can plausibly argue that the spatial resolution in the remaining signal is predominantly due to the phonon channel.

Figure 2c shows the resulting vibrational spectra with the probe positioned on and off the Si dumbbells. Figure 2d shows the integrated intensity of the low and high energy peaks as the probe is moved. The spectral intensity of the 60 meV peak increases by ~40% when the probe is positioned on the column. Figure 2d demonstrates a spatial resolution of better than 2 Å, clearly showing that atomic-resolution vibrational spectroscopy can be accomplished in the forward scattering geometry using the impact signal. The signal from the lower energy peak is noisier, but also shows atomic resolution.

When the collection semi-angle was reduced to 12 mrad, the intensity difference for on and off column probe positions increased to 60% for the 60 meV line scan. Figure 3 shows the spectra and integrated peak intensities as a function of position. Interestingly, while the higher energy signal intensity still tracks with the high-angle annular dark-field (HAADF) signal and peaks on the column, the maximum of the lower energy signal is offset from the column position. Furthermore, in contrast with the large collection angle data, the energies of both peaks change significantly as the probe moves between the columns. The lower energy peak increases in intensity to a maximum as the probe approaches the column, and its energy position shifts from ~40 to 50 meV. The higher energy peak shifts from 60 to 58 meV as the probe moves onto the column. Coherent elastic scattering may cause changes in the absolute intensities of the vibrational signals. For delocalized inelastic scattering processes, this would give no change in the relative intensities of the observed peaks. However, Fig. 3c shows a significant change in relative peak intensities, further demonstrating that the high spatial resolution is substantially associated with a highly localized vibrational excitation process.

For the small collection angle data, the lower energy peak shows an asymmetry in the intensity with respect to the atomic column position, which also correlates with an asymmetry in the bright-field signal entering the spectrometer (Supplementary Fig. 5). Simulations of convergent beam patterns (Supplementary Fig. 5) show that small (~1 mrad) misalignments between the incident cone and the spectrometer entrance aperture, as well as small (~1 mrad) specimen tilts, can introduce an asymmetry to the intensity distribution in the bright-field signal recorded on either side of the atomic columns. Contributions to vibrational spectra from near Brillouin zone boundaries may also be sensitive to small detector shifts or specimen tilts, which may explain the asymmetry we observe.

The low energy peak lies at ~50 meV when the electron probe is located close to the atomic column and is associated with the upper branches between the X and L points of the Brillouin zone (Fig. 1c). When the probe is located between the columns, the energy shifts to ~40 meV, which is associated with other points in the 2D ($\bar{1}$10) section of the Brillouin zone (Supplementary Fig. 3). The change in energy suggests that the dynamical form factor for launching phonons along different directions is strongly influenced by the probe position.

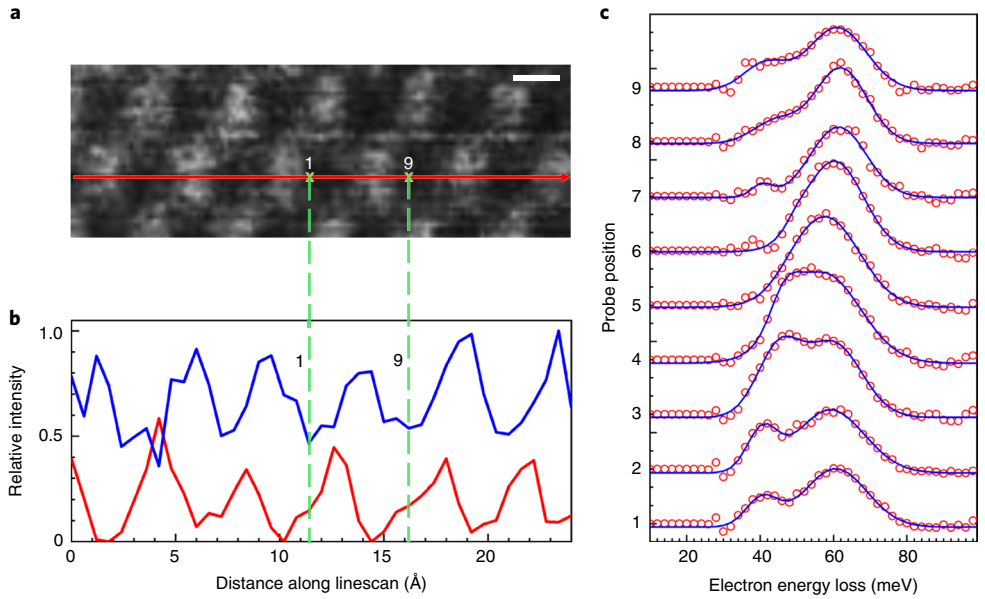


**Fig. 3 | Background subtracted spectra and linescans for small collection angle data. a**, ADF image of Si dumbbells with the monochromator slit inserted to give 16 meV energy resolution. The red arrow indicates the position and direction of EELS linescan acquisition. Scale bar, 2 Å. **b**, The variation in intensity for higher (blue line) and lower (red line) energy phonons over the linescan indicated in **a**. A strong increase in higher energy phonon intensity can be observed around the dumbbell columns. The maxima of the lower energy phonon intensity are offset relative to the dumbbell columns. **c**, Normalized spectra at nine individual probe positions all separated by 0.6 Å along the linescan between labels 1 and 9 in **a** and **b**. Also shown are the two-Gaussian fits (blue lines) to the spectra at all probe positions. The variations in the intensity and shape of the spectra with less than 1 Å shifts in probe position are clear.

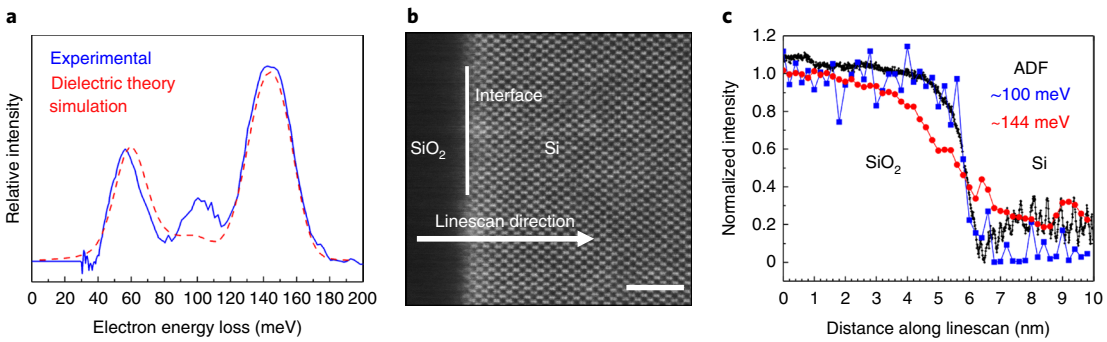


**Fig. 4 | High-resolution vibrational spectroscopy in $SiO_2$. a**, Experimental energy-loss spectrum in $SiO_2$ far from the interface (solid blue line) and a dielectric theory simulation of the spectrum (dashed red line). The peak at ~100 meV does not appear strongly in the dielectric simulation, indicating that it is predominantly excited by impact scattering. **b**, Atomic-resolution ADF image of the $SiO_2$/Si interface (showing the linescan direction across the interface). Scale bar, 2 nm (20 Å). **c**, Normalized signal profiles across the interface—100 meV (blue) and 144 meV (red)—overlaid on the contrast-reversed ADF signal profile. The 100 meV signal traces the ADF signal profile, thereby demonstrating high spatial resolution.

A form of momentum filtering also occurs for the higher energy optical peak and can be interpreted in terms of a simple classical picture where small impact parameter collisions are associated with high momentum transfer. When the probe is on the atomic column (small impact parameter), the peaks shift to 56–58 meV, corresponding to high momentum transfers associated with excitations at the Brillouin zone boundaries. When the probe is positioned between the columns (large impact parameter), the spectral peak appears at ~60 meV, associated with low momentum transfers. Atomic resolution can arise from these low momentum transfer modes with pure elastic scattering followed by a normal phonon scattering process in the first Brillouin zone. Alternatively, it could arise via Umklapp scattering from neighbouring Brillouin zones, without the need for elastic scattering. Given that the sample thickness is on the order of extinction distances (~50 nm) for Bragg beams, it is likely that the resulting signal with atomic resolution is a combination of both possibilities, but a quantitative interpretation of the contributions from normal and Umklapp scattering would require detailed calculations.

High spatial resolution in vibrational EELS is also possible from ionic materials provided impact peaks can be identified. $SiO_2$ exhibits mixed ionic–covalent bonding and the background-subtracted vibrational energy-loss spectrum (Fig. 4a) shows peaks at 58, 100 and 144 meV. The peak at 100 meV corresponds to a mixture of $SiO_4$ stretching and $SiO_4$ bending modes[30]. The signal has a weak dipole component (Fig. 4a) and a significant impact component, which is present in neutron measurements of $SiO_2$ vibrational modes (Supplementary Fig. 4)[30]. The spatial resolution of the $SiO_2$ peaks was explored by performing EELS linescans across a $SiO_2$/Si

interface (see atomic-resolution ADF image in Fig. 4b). The impact component of the 100 meV signal was isolated (by subtracting the dipole component) and all signals were normalized to the total spectral intensity to correct for elastic scattering (Supplementary Fig. 6). The sharpness of the profile from the impact signal is controlled by the abruptness of the $SiO_2$/Si interface. According to dielectric theory, long-range electrostatic interactions and the associated Begrenzungs effect should cause the dipole signal to drop significantly at 20–30 Å from the interface[23]. Linescans of the 144 meV dipole and the 100 meV impact signals are shown in Fig. 4c along with a contrast-reversed ADF signal. The ADF signal variation benchmarks the abruptness and mass thickness changes in the sample near the interface. Whereas the 144 meV dipole signal shows delocalization greater than the 30 Å predicted by dielectric theory, the 100 meV impact signal shows a much sharper profile and follows the ADF signal, demonstrating high spatial resolution. This shows that high spatial resolution is not limited to elemental semiconductors but is possible in all materials (including amorphous materials) that possess peaks where impact scattering dominates over dipole scattering.

In common with other forms of atomic-resolution EELS, a quantitative interpretation of the spatial variations in the vibrational spectrum will require the future development of a theory for coherent inelastic scattering of electrons by lattice and molecular vibrations. However, even the qualitative approach presented here is an important advance that allows the excitation of vibrational modes to be explored with on-axis STEM EELS geometry at atomic resolution. This method can be employed to investigate changes in the character of vibrational modes around atomic-scale structural heterogeneities such as point defects, dislocations and grain boundaries. The ability to probe surface bonding and surface adsorbates should also be possible.

## Online content

Any methods, additional references, Nature Research reporting summaries, source data, statements of code and data availability and associated accession codes are available at https://doi.org/10.1038/s41567-019-0675-5.

Received: 12 August 2019; Accepted: 28 August 2019;
Published online: 7 October 2019

## References

1. Krivanek, O. L. et al. Vibrational spectroscopy in the electron microscope. *Nature* **514**, 209–212 (2014).
2. Miyata, T. et al. Measurement of vibrational spectrum of liquid using monochromated scanning transmission electron microscopy–electron energy loss spectroscopy. *Microscopy* **63**, 377–382 (2014).
3. Rez, P. Is localized infrared spectroscopy now possible in the electron microscope? *Microsc. Microanal.* **20**, 671–677 (2014).
4. Hage, F. S., Kepaptsoglou, D. M., Ramasse, Q. M. & Allen, L. J. Phonon spectroscopy at atomic resolution. *Phys. Rev. Lett.* **122**, 016103 (2019).
5. Lagos, M. J., Trugler, A., Hohenester, U. & Batson, P. E. Mapping vibrational surface and bulk modes in a single nanocube. *Nature* **543**, 529–532 (2017).
6. Govyadinov, A. A. et al. Probing low-energy hyperbolic polaritons in van der Waals crystals with an electron microscope. *Nat. Commun.* **8**, 95 (2017).
7. Idrobo, J. C. et al. Temperature measurement by a nanoscale electron probe using energy gain and loss spectroscopy. *Phys. Rev. Lett.* **120**, 09590 (2018).
8. Lagos, M. J. & Batson, P. E. Thermometry with subnanometer resolution in the electron microscope using the principle of detailed balancing. *Nano Lett.* **18**, 4556–4563 (2018).
9. Hage, F. S. et al. Nanoscale momentum-resolved vibrational spectroscopy. *Sci. Adv.* **4**, eaar7495 (2018).
10. Jokisaari, J. R. et al. Vibrational spectroscopy of water with high spatial resolution. *Adv. Mater.* **30**, 1802702 (2018).
11. Rez, P. et al. Damage-free vibrational spectroscopy of biological materials in the electron microscope. *Nat. Commun.* **7**, 10945 (2016).
12. Haiber, D. & Crozier, P. A. Nanoscale probing of local hydrogen heterogeneity in disordered carbon nitrides with vibrational EELS. *ACS Nano* **12**, 5463–5472 (2018).
13. Crozier, P. A., Aoki, T. & Liu, Q. Detection of water and its derivatives on individual nanoparticles using vibrational electron energy-loss spectroscopy. *Ultramicroscopy* **169**, 30–36 (2016).
14. Egerton, R. F. Prospects for vibrational-mode EELS with high spatial resolution. *Microsc. Microanal.* **20**, 658–663 (2014).
15. Forbes, B. D. & Allen, L. J. Modeling energy-loss spectra due to phonon excitation. *Phys. Rev. B* **94**, 014110 (2016).
16. Dwyer, C. Localization of high-energy electron scattering from atomic vibrations. *Phys. Rev. B* **89**, 054103 (2014).
17. Rez, P. Does phonon scattering give high-resolution images? *Ultramicroscopy* **52**, 260–266 (1993).
18. Hohenester, U., Trügler, A., Batson, P. E. & Lagos, M. J. Inelastic vibrational bulk and surface losses of swift electrons in ionic nanostructures. *Phys. Rev. B* **97**, 165418 (2018).
19. Spence, J. C. H. *High Resolution Electron Microscopy* 3rd edn (Oxford Science Publications, 2003).
20. Cowley, J. M. Image contrast in a transmission scanning electron microscope. *Appl. Phys. Lett.* **15**, 58–59 (1969).
21. Ibach, H. & Mills, D. L. *Electron Energy Loss Spectroscopy and Surface Vibrations* (Academic Press, 1982).
22. Crozier, P. A. Vibrational and valence aloof beam EELS: a potential tool for nondestructive characterization of nanoparticle surfaces. *Ultramicroscopy* **180**, 104–114 (2017).
23. Venkatraman, K., Rez, P., March, K. & Crozier, P. A. The influence of surfaces and interfaces on high spatial resolution vibrational EELS from $SiO_2$. *Microscopy* **67**, i14–i23 (2018).
24. Dwyer, C. et al. Electron-beam mapping of vibrational modes with nanometer spatial resolution. *Phys. Rev. Lett.* **117**, 256101 (2016).
25. Jain, A. et al. Commentary: The Materials Project: a materials genome approach to accelerating materials innovation. *APL Mater.* **1**, 011002 (2013).
26. Ong, S. P. et al. Python Materials Genomics (pymatgen): a robust, open-source python library for materials analysis. *Comput. Mater. Sci.* **68**, 314–319 (2013).
27. Dolling, G. *Lattice Vibrations in Crystals with the Diamond Structure* (Atomic Energy of Canada Ltd, 1962).
28. Ashcroft, N. W. & Mermin, N. D. *Solid State Physics* (W.B. Saunders Company, 1976).
29. Kulda, J., Strauch, D., Pavone, P. & Ishii, Y. Inelastic-neutron-scattering study of phonon eigenvectors and frequencies in Si. *Phys. Rev. B* **50**, 13347 (1994).
30. Haworth, R., Mountjoy, G., Corno, M., Ugliengo, P. & Newport, R. J. Probing vibrational modes in silica glass using inelastic neutron scattering with mass contrast. *Phys. Rev. B* **81**, 060301 (2010).

## Acknowledgements

Financial support for K.V., B.D.A.L., P.R. and P.A.C. was provided by the US National Science Foundation (grant no. CHE-1508667) and for B.D.A.L. and P.A.C. by the US Department of Energy (grant no. DE-SC0004954). We also acknowledge the use of (S)TEM at John M. Cowley Center for High Resolution Electron Microscopy in the Eyring Materials Center at Arizona State University. P.A.C. acknowledges stimulating discussions on atomic-resolution vibrational spectroscopy with L. Allen. We acknowledge assistance from A. Singh in the use of Phonopy.

## Author contributions

K.V. prepared samples. K.V. and K.M. acquired all experimental vibrational EELS data. B.D.A.L. developed software for spectral processing. K.V. and B.D.A.L. analysed the EELS results. B.D.A.L. performed simulations of convergent beam electron diffraction (CBED) patterns. K.V. performed dielectric theory simulations. P.R. developed and interpreted phonon models. P.A.C. and P.R. initiated the project and were involved in extensive discussions on the interpretation of the results. All authors were active in writing the manuscript.

## Competing interests

The authors declare no competing interests.

## Additional information

**Supplementary information** is available for this paper at https://doi.org/10.1038/s41567-019-0675-5.

**Correspondence and requests for materials** should be addressed to P.A.C.

**Peer review information** *Nature Physics* thanks Robert Klie and the other, anonymous, reviewer(s) for their contribution to the peer review of this work.

**Reprints and permissions information** is available at www.nature.com/reprints.

**Publisher's note** Springer Nature remains neutral with regard to jurisdictional claims in published maps and institutional affiliations.

## Methods

**Sample preparation.** To investigate vibrational spectra in Si, a conventional cross-section Si sample in a [$\bar{1}$10] zone axis orientation was prepared by dimpling and ion milling. A second sample was prepared to investigate the Si/$SiO_2$ interface. The top surface of a Si wafer was subjected to thermal oxidation at 900 °C to obtain a ~3 µm film of $SiO_2$ on the Si substrate. The oxidized wafer was then prepared for STEM EELS analysis by performing a lift-out procedure using a Ga-ion beam and an Omniprobe on a Nova 200 NanoLab (FEI) focused ion beam (FIB) combined with a scanning electron microscope (SEM). The thickness of the lift-out specimen measured using SEM approached ~100 nm near the edges and ~80 nm near the $SiO_2$/Si interface. The interface plane normal was parallel to the (001) crystallographic plane in Si while the zone axis was along the [110] crystallographic direction in Si.

**Monochromated STEM-EELS measurements.** STEM EELS analysis was performed on all samples using a NION HERMES UltraSTEM 100 aberration-corrected electron microscope equipped with a monochromator, operated at 60 kV. The probe convergence semi-angle was 28 mrad, and the corresponding collection semi-angles were 12 and 24 mrad. To record spectra, a dispersion of 1 or 2 meV per channel was used with the 12 mrad collection angle and 0.37 meV per channel was used with the 24 mrad collection angle. Aberration correction of the magnetic lenses up to the fifth order produced probes of ~0.12 nm diameter with beam currents of ~100 pA. During the monochromated experiment, the beam current was ~10 pA, and the energy resolution was 15 meV for the 12 mrad collection angle and 10 meV for the 24 mrad collection angle. The monochromated probe size was estimated to be ~0.17 nm.

**Background fitting to vibrational EELS spectra.** All acquired spectra were processed using the Gatan Microscopy Suite, the FIJI-Cornell Spectrum Imager[31] and custom-written MATLAB code. The spectra were calibrated first by using cross-correlation to align the centre of the ZLPs to 0 meV. All spectra were then normalized to the total intensity entering the spectrometer.

The characteristic vibrational peaks sit on a rapidly falling background arising from both non-characteristic phonon losses and a tail on the zero-loss peak. The signal-to-background ratio is typically 10–20%, making accurate background modelling and correction critical to reveal subtle differences in the characteristic peak shapes and intensities. Background subtraction in previous studies on vibrational EELS has typically involved fitting a power-law or polynomial function to the data using two fitting windows, one placed immediately before and one placed immediately after the vibrational peak of interest. Earlier work on low-loss EELS has tested several functions that can be used to approximate the form of the ZLP itself[32], finding the Pseudo-Voigt function (the sum of a Gaussian and a Lorentzian) to be particularly well suited.

In this work, we also used a two-window method for background fitting. We tested the exponential, power-law and linear combination of power-laws (LCPL) functions because these have traditionally been used for background subtraction in EELS[31]. In addition, we tested the Pseudo-Voigt and Pearson VII functions (essentially a Lorentzian raised to a power)[33] because these can be used to model spectral peaks, and we hypothesized that they might be superior functions to fit to the tail of the ZLP than exponential or power-law functions. When processing our experimental data, the most appropriate function for background subtraction was chosen based on three main criteria:

- Minimization of a reduced $\chi^2$ value for the fit within the fitting windows (using the square root of the number of counts as a crude approximation of the noise)
- Inspection of spectra to ensure that the intensities in signal channels are positive after background subtraction (negative intensity is unphysical and results from a background model that has overestimated the true background)
- Robustness of background subtraction when changing the position and width of the fitting windows (a significant drop in fit quality when repositioning windows is indicative of a poor background model)

For silicon, we found that the Pseudo-Voigt function outperformed the other fitting models, because it resulted in fewer background subtracted spectra with regions of negative intensity and was more robust to changes in the width and position of fitting windows.

For linescans across the Si/$SiO_2$ interface, we found the Pearson VII function to be the most robust background model because it did not leave a region of significant negative intensity after background subtraction between the vibrational peaks at ~58 and 144 meV when the probe was positioned at the interface. In this case, the fitting windows had to be spaced much further apart than they were for the spectra from Si, which may make accurate background fitting more challenging.

The MATLAB codes used to fit backgrounds are uploaded to B.D.A.L.'s GitHub page (https://github.com/bdalevin).

**Gaussian fitting to background-subtracted Si vibrational spectra.** After background subtraction, we modelled the variation in the intensity of vibrational spectra from Si using a simple two-Gaussian peak fitting model. Each Gaussian was constrained to have widths of up to a maximum of 40 meV, because this was the energy range over which the vibrational spectra of interest lay. A lower limit for Gaussian width was chosen based on the energy resolution of our measurements (10 meV when using a larger collection angle and 15 meV when using a smaller collection angle). The peak positions were constrained to lie in the ranges 55–63 meV and 40–50 meV to model the higher and lower energy phonon dispersion branches in Si, as indicated in Fig. 1c.

The MATLAB code used to fit Gaussians to the spectra are uploaded to B.D.A.L.'s GitHub page (https://github.com/bdalevin).

**Calculating the phonon dispersion surfaces.** The 2D dispersion surfaces were calculated with a combination of Phonopy and VASP using a 4×4×4 supercell based on the primitive Si unit cell. The VASP calculations were converged to $1.0\times10^{-8}$ eV with PAW potentials. Phonon frequencies were calculated on a grid of 307 points spanning one quadrant of the $\bar{1}$10 2D Brillouin zone[34–36].

**Theoretical model.** The specimen thicknesses where measurements were performed were on the order of 50 nm, which is similar to the extinction distance for Si (110) (~55 nm). There is therefore dynamical elastic diffraction both before and after the phonon scattering. In many ways the process is similar to HAADF, where lattice resolution is achieved by coherent interference in the incident probe, followed by transfer to a detector by multi-phonon (thermal diffuse) scattering[37]. In this case, the transfer is to the range of angles and energies selected by the spectrometer, by both acoustic and optic phonons. The phonon intensity when the probe is at position $r_p$ is an integral over contributions from slices of thickness d$z$ at depth $z$ in a specimen of thickness $t$:

$$\begin{aligned} I(\mathbf{r_p}) = \sum_{L,L',g,g',h,h'} \iint & Q_{0L}(\mathbf{q}',t-z)Q^*_{0L'}(\mathbf{q}',t-z) \\ & \times H(\mathbf{q}'+\mathbf{L}-\mathbf{g}-\mathbf{q})H^*(\mathbf{q}'+\mathbf{L}'-\mathbf{g}'-\mathbf{q}) \\ & \times P_{gh}(\mathbf{q},z)P^*_{g'h'}(\mathbf{q},z)A(\mathbf{q}+\mathbf{h})A(\mathbf{q}+\mathbf{h}')\exp\left[-i(\mathbf{h}-\mathbf{h}')\mathbf{r_p}\right]\mathrm{d}\mathbf{q}'\mathrm{d}\mathbf{q}\mathrm{d}z \end{aligned} \quad (1)$$

where $\mathbf{q}'$ represents the wavevector in the Brillouin zone characterizing the final state accepted by the spectrometer, $\mathbf{q}$ is the wavevector in the Brillouin zone representing the initial state (Fig. 1), $\mathbf{q}'-\mathbf{q}$ is the phonon wavevector $\mathbf{L},\mathbf{L}'$, $\mathbf{g},\mathbf{g}'$, $\mathbf{h},\mathbf{h}'$ are reciprocal lattice vectors, $A(\mathbf{q}+\mathbf{h})$ is an aperture function defining the incident probe, $P_{\mathbf{gh}}(\mathbf{q},z)$ represents dynamical propagation of the incident electron wave before the phonon scattering, which is represented by $H(\mathbf{q}'+\mathbf{L}-\mathbf{g}-\mathbf{q}')$, and $Q_{0L}(\mathbf{q}',t-z)$ represents the dynamical scattering of the phonon scattered electrons.

The scattering operator for phonons is given by

$$H(\mathbf{q}+\mathbf{g}) = (\mathbf{q}+\mathbf{g})\cdot\mathbf{e}\left(\frac{\hbar}{2M\omega(q)}\right)^{\frac{1}{2}} f_{el}(q+g)(1+\exp(i\mathbf{q}\cdot\mathbf{R})) \quad (2)$$

where $f_{el}(q+g)$ is the electron scattering factor, $\mathbf{R}$ is the position of the second atom in the primitive cell, $M$ is the mass of the atom, $\omega(q)$ is the frequency and $\mathbf{e}$ is the polarization direction. We have assumed that energies that can be resolved by our spectrometer are greater than $k_BT$ (25 meV) and only phonon creation processes need be considered. In a Bloch wave picture the dynamical diffraction propagation matrices can be expressed as

$$P_{gh}(q,z) = \sum\nolimits_j C_g^j \exp(ik_jz)C_h^{*j} \quad (3)$$

where $k_j$ are the eigenvalues and $C_g^j$ are the eigenvectors. Alternatively, the propagation matrix can be calculated by the multislice method.

In the simplified theory we will neglect the dynamical elastic scattering before and after the phonon scattering, and assume that just three beams contribute to the image $-g,0,g$ (in Si these could be (111) beams). Neglecting cross-aperture interference, we have

$$\Delta q = q\prime - q$$

which is the net phonon momentum transfer.

The simplified intensity $I(r_p)$ is given by

$$\begin{aligned} I(r_p) = \iint & \left(\tfrac{2\hbar}{\omega M}\right)\cos^2(\Delta qR_p) \\ & \begin{bmatrix} f(\Delta q+g)f(\Delta q)((\Delta\mathbf{q}+\mathbf{g})\cdot\mathbf{e})(\Delta\mathbf{q}\cdot\mathbf{e})\exp(-i\mathbf{g}\cdot\mathbf{r}_p) \\ +f(\Delta q-g)f(\Delta q)((\Delta\mathbf{q}-\mathbf{g})\cdot\mathbf{e})(\Delta\mathbf{q}\cdot\mathbf{e})\exp(i\mathbf{g}\cdot\mathbf{r}_p) \\ (\Delta\mathbf{q}\cdot\mathbf{e})^2f^2(\Delta q) \end{bmatrix}\Delta q \end{aligned} \quad (4)$$

which can be rewritten as an expression inversely proportional to the phonon energy, $E$, and a density of phonon states:

$$\begin{aligned} I(r_p) = \iint & \left(\tfrac{2\hbar^2}{M}\right)\cos^2(\Delta qR_p) \\ & \begin{bmatrix} f(\Delta q+g)f(\Delta q)((\Delta\mathbf{q}+\mathbf{g})\cdot\mathbf{e})(\Delta\mathbf{q}\cdot\mathbf{e})\exp(-i\mathbf{g}\cdot\mathbf{r}_p) \\ +f(\Delta q-g)f(\Delta q)((\Delta\mathbf{q}-\mathbf{g})\cdot\mathbf{e})(\Delta\mathbf{q}\cdot\mathbf{e})\exp(i\mathbf{g}\cdot\mathbf{r}_p) \\ (\Delta\mathbf{q}\cdot\mathbf{e})^2f^2(\Delta q) \end{bmatrix}\tfrac{1}{E}\tfrac{\mathrm{d}E}{|\nabla E(\Delta q)|} \end{aligned} \quad (5)$$

Note that if there is a slight tilt such that the first two terms in the square brackets are not equal then there will be a change in the peak phonon intensity with respect to $r_p$.

## Data availability

The experimental linescans and simultaneously acquired ADF signals analysed in this work have been uploaded to the Figshare repository. The data can be found at https://doi.org/10.6084/m9.figshare.c.4621640. Files have been uploaded in the easily readable 32-bit.tif image format. The data represented in Figs. 1b, 2c,d, 3b,c and 4a,c are available as Supplementary information files.

## Code availability

All of the MATLAB codes used to analyse the data are uploaded to B.D.A.L.'s GitHub page (https://github.com/bdalevin) under the repository titled 'Background-Modelling-EELS-MATLAB-Code'.

## References

31. Cueva, P., Hovden, R., Mundy, J. A., Xin, H. L. & Muller, D. A. Data processing for atomic resolution electron energy loss spectroscopy. *Microsc. Microanal.* **18**, 667–675 (2012).
32. Zhu, J. T., Crozier, P. A., Ercius, P. & Anderson, J. R. Derivation of optical properties of carbonaceous aerosols by monochromated electron energy-loss spectroscopy. *Microsc. Microanal.* **20**, 748–759 (2014).
33. Hall, M., Veeraraghavan, V., Rubin, H. & Winchell, P. The approximation of symmetric X-ray peaks by Pearson type VII distributions. *J. Appl. Crystallogr.* **10**, 66–68 (1977).
34. Kresse, G. & Furthmüller, J. Efficient iterative schemes for ab initio total-energy calculations using a plane-wave basis set. *Phys. Rev. B* **54**, 11169–11186 (1996).
35. Kresse, G. & Joubert, D. From ultrasoft pseudopotentials to the projector augmented-wave method. *Phys. Rev. B* **59**, 1758–1775 (1999).
36. Togo, A. & Tanaka, I. First principles phonon calculations in materials science. *Scr. Mater.* **108**, 1–5 (2015).
37. Amali, A. & Rez, P. Theory of lattice resolution in high-angle annular dark-field images. *Microsc. Microanal.* **3**, 28–46 (1997).